

Nuclear-modification factor of charged hadrons at forward and backward rapidity in $p+\text{Al}$ and $p+\text{Au}$ collisions at $\sqrt{s_{NN}} = 200 \text{ GeV}$

C. Aidala,⁴⁰ Y. Akiba,^{52, 53}, * M. Alfred,²² V. Andrieux,⁴⁰ N. Apadula,²⁷ H. Asano,^{33, 52} B. Azmoun,⁷ V. Babintsev,²³ N.S. Bandara,³⁹ K.N. Barish,⁸ S. Bathe,^{5, 53} A. Bazilevsky,⁷ M. Beaumier,⁸ R. Belmont,^{11, 46} A. Berdnikov,⁵⁵ Y. Berdnikov,⁵⁵ D.S. Blau,^{32, 43} J.S. Bok,⁴⁵ M.L. Brooks,³⁵ J. Bryslawskyj,^{5, 8} V. Bumazhnov,²³ S. Campbell,¹² V. Canoa Roman,⁵⁸ R. Cervantes,⁵⁸ C.Y. Chi,¹² M. Chiu,⁷ I.J. Choi,²⁴ J.B. Choi,^{29, †} Z. Citron,⁶³ M. Connors,^{20, 53} N. Cronin,⁵⁸ M. Csand,¹⁵ T. Cs  rg  ,^{16, 64} T.W. Danley,⁴⁷ M.S. Daugherty,¹ G. David,^{7, 14, 58} K. DeBlasio,⁴⁴ K. Dehmelt,⁵⁸ A. Denisov,²³ A. Deshpande,^{7, 53, 58} E.J. Desmond,⁷ A. Dion,⁵⁸ D. Dixit,⁵⁸ J.H. Do,⁶⁵ A. Drees,⁵⁸ K.A. Drees,⁶ J.M. Durham,³⁵ A. Durum,²³ A. Enokizono,^{52, 54} H. En'yo,⁵² S. Esumi,⁶¹ B. Fadem,⁴¹ W. Fan,⁵⁸ N. Feege,⁵⁸ D.E. Fields,⁴⁴ M. Finger,⁹ M. Finger, Jr.,⁹ S.L. Fokin,³² J.E. Frantz,⁴⁷ A. Franz,⁷ A.D. Frawley,¹⁹ Y. Fukuda,⁶¹ C. Gal,⁵⁸ P. Gallus,¹³ E.A. Gamez,⁴⁰ P. Garg,^{3, 58} H. Ge,⁵⁸ F. Giordano,²⁴ Y. Goto,^{52, 53} N. Grau,² S.V. Greene,⁶² M. Grosse Perdekamp,²⁴ T. Gunji,¹⁰ H. Guragain,²⁰ T. Hachiya,^{42, 52, 53} J.S. Haggerty,⁷ K.I. Hahn,¹⁷ H. Hamagaki,¹⁰ H.F. Hamilton,¹ S.Y. Han,^{17, 52} J. Hanks,⁵⁸ S. Hasegawa,²⁸ T.O.S. Haseler,²⁰ X. He,²⁰ T.K. Hemmick,⁵⁸ J.C. Hill,²⁷ K. Hill,¹¹ A. Hodges,²⁰ R.S. Hollis,⁸ K. Homma,²¹ B. Hong,³¹ T. Hoshino,²¹ N. Hotvedt,²⁷ J. Huang,⁷ S. Huang,⁶² K. Imai,²⁸ M. Inaba,⁶¹ A. Iordanova,⁸ D. Isenhower,¹ S. Ishimaru,⁴² D. Ivanishchev,⁵¹ B.V. Jacak,⁵⁸ M. Jezghani,²⁰ Z. Ji,⁵⁸ X. Jiang,³⁵ B.M. Johnson,^{7, 20} D. Jouan,⁴⁹ D.S. Jumper,²⁴ J.H. Kang,⁶⁵ D. Kapukchyan,⁸ S. Karthas,⁵⁸ D. Kawall,³⁹ A.V. Kazantsev,³² V. Khachatryan,⁵⁸ A. Khanzadeev,⁵¹ A. Khatiwada,³⁵ C. Kim,^{8, 31} E.-J. Kim,²⁹ M. Kim,^{52, 56} D. Kincses,¹⁵ E. Kistenev,⁷ J. Klatsky,¹⁹ P. Kline,⁵⁸ T. Koblesky,¹¹ D. Kotov,^{51, 55} S. Kudo,⁶¹ B. Kurylis,¹⁵ K. Kurita,⁵⁴ Y. Kwon,⁶⁵ J.G. Lajoie,²⁷ A. Lebedev,²⁷ S. Lee,⁶⁵ S.H. Lee,^{27, 58} M.J. Leitch,³⁵ Y.H. Leung,⁵⁸ N.A. Lewis,⁴⁰ X. Li,³⁵ S.H. Lim,^{35, 65} M.X. Liu,³⁵ V.-R. Loggins,²⁴ S. L  k  s,^{15, 16} K. Lovasz,¹⁴ D. Lynch,⁷ T. Majoros,¹⁴ Y.I. Makdisi,⁶ M. Makek,⁶⁶ V.I. Manko,³² E. Mannel,⁷ M. McCumber,³⁵ P.L. McGaughey,³⁵ D. McGlinchey,^{11, 35} C. McKinney,²⁴ M. Mendoza,⁸ W.J. Metzger,¹⁶ A.C. Mignerey,³⁸ A. Milov,⁶³ D.K. Mishra,⁴ J.T. Mitchell,⁷ Iu. Mitrankov,⁵⁵ G. Mitsuka,^{30, 52, 53} S. Miyasaka,^{52, 60} S. Mizuno,^{52, 61} P. Montuenga,²⁴ T. Moon,⁶⁵ D.P. Morrison,⁷ S.I. Morrow,⁶² T. Murakami,^{33, 52} J. Murata,^{52, 54} K. Nagai,⁶⁰ K. Nagashima,^{21, 52} T. Nagashima,⁵⁴ J.L. Nagle,¹¹ M.I. Nagy,¹⁵ I. Nakagawa,^{52, 53} K. Nakano,^{52, 60} C. Nattrass,⁵⁹ S. Nelson,¹⁸ T. Niida,⁶¹ R. Nishitani,⁴² R. Nouicer,^{7, 53} T. Nov  k,^{16, 64} N. Novitzky,⁵⁸ A.S. Nyanin,³² E. O'Brien,⁷ C.A. Ogilvie,²⁷ J.D. Orjuela Koop,¹¹ J.D. Osborn,⁴⁰ A. Oskarsson,³⁶ G.J. Ottino,⁴⁴ K. Ozawa,^{30, 61} V. Pantuev,²⁵ V. Papavassiliou,⁴⁵ J.S. Park,⁵⁶ S. Park,^{52, 56, 58} S.F. Pate,⁴⁵ M. Patel,²⁷ W. Peng,⁶² D.V. Perepelitsa,^{7, 11} G.D.N. Perera,⁴⁵ D.Yu. Peressounko,³² C.E. PerezLara,⁵⁸ J. Perry,²⁷ R. Petti,⁷ M. Phipps,^{7, 24} C. Pinkenburg,⁷ R.P. Pisani,⁷ A. Pun,⁴⁷ M.L. Purschke,⁷ P.V. Radzevich,⁵⁵ K.F. Read,^{48, 59} D. Reynolds,⁵⁷ V. Riabov,^{43, 51} Y. Riabov,^{51, 55} D. Richford,⁵ T. Rinn,²⁷ S.D. Rolnick,⁸ M. Rosati,²⁷ Z. Rowan,⁵ J. Runchey,²⁷ A.S. Safonov,⁵⁵ T. Sakaguchi,⁷ H. Sako,²⁸ V. Samsonov,^{43, 51} M. Sarsour,²⁰ S. Sato,²⁸ C.Y. Scarlett,¹⁸ B. Schaefer,⁶² B.K. Schmoll,⁵⁹ K. Sedgwick,⁸ R. Seidl,^{52, 53} A. Sen,^{27, 59} R. Seto,⁸ A. Sexton,³⁸ D. Sharma,⁵⁸ I. Shein,²³ T.-A. Shibata,^{52, 60} K. Shigaki,²¹ M. Shimomura,^{27, 42} T. Shioya,⁶¹ P. Shukla,⁴ A. Sickles,²⁴ C.L. Silva,³⁵ D. Silvermyr,³⁶ B.K. Singh,³ C.P. Singh,³ V. Singh,³ M.J. Skoby,⁴⁰ M. Slune  ka,⁹ K.L. Smith,¹⁹ M. Snowball,³⁵ R.A. Soltz,³⁴ W.E. Sondheim,³⁵ S.P. Sorensen,⁵⁹ I.V. Sourikova,⁷ P.W. Stankus,⁴⁸ S.P. Stoll,⁷ T. Sugitate,²¹ A. Sukhanov,⁷ T. Sumita,⁵² J. Sun,⁵⁸ Z. Sun,¹⁴ S. Suzuki,⁴² J. Sziklai,⁶⁴ K. Tanida,^{28, 53, 56} M.J. Tannenbaum,⁷ S. Tarafdar,^{62, 63} A. Taranenko,⁴³ G. Tarnai,¹⁴ R. Tieulent,^{20, 37} A. Timilsina,²⁷ T. Todoroki,^{53, 61} M. Tom  sek,¹³ C.L. Towell,¹ R.S. Towell,¹ I. Tserruya,⁶³ Y. Ueda,²¹ B. Ujvari,¹⁴ H.W. van Hecke,³⁵ J. Velkovska,⁶² M. Virius,¹³ V. Vrba,^{13, 26} N. Vukman,⁶⁶ X.R. Wang,^{45, 53} Z. Wang,⁵ Y.S. Watanabe,¹⁰ C.P. Wong,²⁰ C.L. Woody,⁷ C. Xu,⁴⁵ Q. Xu,⁶² L. Xue,²⁰ S. Yalcin,⁵⁸ Y.L. Yamaguchi,^{53, 58} H. Yamamoto,⁶¹ A. Yanovich,²³ J.H. Yoo,^{31, 53} I. Yoon,⁵⁶ H. Yu,^{45, 50} I.E. Yushmanov,³² W.A. Zajc,¹² A. Zelenski,⁶ Y. Zhai,²⁷ S. Zharko,⁵⁵ and L. Zou⁸

(PHENIX Collaboration)

¹Abilene Christian University, Abilene, Texas 79699, USA

²Department of Physics, Augustana University, Sioux Falls, South Dakota 57197, USA

³Department of Physics, Banaras Hindu University, Varanasi 221005, India

⁴Bhabha Atomic Research Centre, Bombay 400 085, India

⁵Baruch College, City University of New York, New York, New York, 10010 USA

⁶Collider-Accelerator Department, Brookhaven National Laboratory, Upton, New York 11973-5000, USA

⁷Physics Department, Brookhaven National Laboratory, Upton, New York 11973-5000, USA

⁸University of California-Riverside, Riverside, California 92521, USA

⁹Charles University, Ovocn   trh 5, Praha 1, 116 36, Prague, Czech Republic

¹⁰Center for Nuclear Study, Graduate School of Science, University of Tokyo, 7-3-1 Hongo, Bunkyo, Tokyo 113-0033, Japan

¹¹University of Colorado, Boulder, Colorado 80309, USA

¹²*Columbia University, New York, New York 10027 and Nevis Laboratories, Irvington, New York 10533, USA*

¹³*Czech Technical University, Zikova 4, 166 36 Prague 6, Czech Republic*

¹⁴*Debrecen University, H-4010 Debrecen, Egyetem tér 1, Hungary*

¹⁵*ELTE, Eötvös Loránd University, H-1117 Budapest, Pázmány P. s. 1/A, Hungary*

¹⁶*Eszterházy Károly University, Károly Róbert Campus, H-3200 Gyöngyös, Mátrai út 36, Hungary*

¹⁷*Ewha Womans University, Seoul 120-750, Korea*

¹⁸*Florida A&M University, Tallahassee, FL 32307, USA*

¹⁹*Florida State University, Tallahassee, Florida 32306, USA*

²⁰*Georgia State University, Atlanta, Georgia 30303, USA*

²¹*Hiroshima University, Kagamiyama, Higashi-Hiroshima 739-8526, Japan*

²²*Department of Physics and Astronomy, Howard University, Washington, DC 20059, USA*

²³*IHEP Protvino, State Research Center of Russian Federation, Institute for High Energy Physics, Protvino, 142281, Russia*

²⁴*University of Illinois at Urbana-Champaign, Urbana, Illinois 61801, USA*

²⁵*Institute for Nuclear Research of the Russian Academy of Sciences, prospekt 60-letiya Oktyabrya 7a, Moscow 117312, Russia*

²⁶*Institute of Physics, Academy of Sciences of the Czech Republic, Na Slovance 2, 182 21 Prague 8, Czech Republic*

²⁷*Iowa State University, Ames, Iowa 50011, USA*

²⁸*Advanced Science Research Center, Japan Atomic Energy Agency, 2-4 Shirakata Shirane, Tokai-mura, Naka-gun, Ibaraki-ken 319-1195, Japan*

²⁹*Jeonbuk National University, Jeonju, 54896, Korea*

³⁰*KEK, High Energy Accelerator Research Organization, Tsukuba, Ibaraki 305-0801, Japan*

³¹*Korea University, Seoul, 02841*

³²*National Research Center “Kurchatov Institute”, Moscow, 123098 Russia*

³³*Kyoto University, Kyoto 606-8502, Japan*

³⁴*Lawrence Livermore National Laboratory, Livermore, California 94550, USA*

³⁵*Los Alamos National Laboratory, Los Alamos, New Mexico 87545, USA*

³⁶*Department of Physics, Lund University, Box 118, SE-221 00 Lund, Sweden*

³⁷*IPNL, CNRS/IN2P3, Univ Lyon, Université Lyon 1, F-69622, Villeurbanne, France*

³⁸*University of Maryland, College Park, Maryland 20742, USA*

³⁹*Department of Physics, University of Massachusetts, Amherst, Massachusetts 01003-9337, USA*

⁴⁰*Department of Physics, University of Michigan, Ann Arbor, Michigan 48109-1040, USA*

⁴¹*Muhlenberg College, Allentown, Pennsylvania 18104-5586, USA*

⁴²*Nara Women’s University, Kita-uoya Nishi-machi Nara 630-8506, Japan*

⁴³*National Research Nuclear University, MEPhI, Moscow Engineering Physics Institute, Moscow, 115409, Russia*

⁴⁴*University of New Mexico, Albuquerque, New Mexico 87131, USA*

⁴⁵*New Mexico State University, Las Cruces, New Mexico 88003, USA*

⁴⁶*Physics and Astronomy Department, University of North Carolina at Greensboro, Greensboro, North Carolina 27412, USA*

⁴⁷*Department of Physics and Astronomy, Ohio University, Athens, Ohio 45701, USA*

⁴⁸*Oak Ridge National Laboratory, Oak Ridge, Tennessee 37831, USA*

⁴⁹*IPN-Orsay, Univ. Paris-Sud, CNRS/IN2P3, Université Paris-Saclay, BP1, F-91406, Orsay, France*

⁵⁰*Peking University, Beijing 100871, People’s Republic of China*

⁵¹*PNPI, Petersburg Nuclear Physics Institute, Gatchina, Leningrad region, 188300, Russia*

⁵²*RIKEN Nishina Center for Accelerator-Based Science, Wako, Saitama 351-0198, Japan*

⁵³*RIKEN BNL Research Center, Brookhaven National Laboratory, Upton, New York 11973-5000, USA*

⁵⁴*Physics Department, Rikkyo University, 3-34-1 Nishi-Ikebukuro, Toshima, Tokyo 171-8501, Japan*

⁵⁵*Saint Petersburg State Polytechnic University, St. Petersburg, 195251 Russia*

⁵⁶*Department of Physics and Astronomy, Seoul National University, Seoul 151-742, Korea*

⁵⁷*Chemistry Department, Stony Brook University, SUNY, Stony Brook, New York 11794-3400, USA*

⁵⁸*Department of Physics and Astronomy, Stony Brook University, SUNY, Stony Brook, New York 11794-3800, USA*

⁵⁹*University of Tennessee, Knoxville, Tennessee 37996, USA*

⁶⁰*Department of Physics, Tokyo Institute of Technology, Oh-okayama, Meguro, Tokyo 152-8551, Japan*

⁶¹*Tomonaga Center for the History of the Universe, University of Tsukuba, Tsukuba, Ibaraki 305, Japan*

⁶²*Vanderbilt University, Nashville, Tennessee 37235, USA*

⁶³*Weizmann Institute, Rehovot 76100, Israel*

⁶⁴*Institute for Particle and Nuclear Physics, Wigner Research Centre for Physics, Hungarian Academy of Sciences (Wigner RCP, RMKI) H-1525 Budapest 114, POBox 49, Budapest, Hungary*

⁶⁵*Yonsei University, IPAP, Seoul 120-749, Korea*

⁶⁶*Department of Physics, Faculty of Science, University of Zagreb, Bijenička c. 32 HR-10002 Zagreb, Croatia*

(Dated: February 26, 2020)

The PHENIX experiment has studied nuclear effects in $p+Al$ and $p+Au$ collisions at $\sqrt{s_{NN}} = 200$ GeV on charged hadron production at forward rapidity ($1.4 < \eta < 2.4$, p -going direction) and backward rapidity ($-2.2 < \eta < -1.2$, A -going direction). Such effects are quantified by measuring nuclear modification factors as a function of transverse momentum and pseudorapidity in various collision multiplicity selections. In central $p+Al$ and $p+Au$ collisions, a suppression (enhancement)

is observed at forward (backward) rapidity compared to the binary scaled yields in $p+p$ collisions. The magnitude of enhancement at backward rapidity is larger in $p+\text{Au}$ collisions than in $p+\text{Al}$ collisions, which have a smaller number of participating nucleons. However, the results at forward rapidity show a similar suppression within uncertainties. The results in the integrated centrality are compared with calculations using nuclear parton distribution functions, which show a reasonable agreement at the forward rapidity but fail to describe the backward rapidity enhancement.

I. INTRODUCTION

Measurements of particle production in heavy-ion collisions enable the study of properties of a hot and dense nuclear medium called the quark-gluon plasma (QGP) [1–4]. An initial striking observation at the Relativistic Heavy Ion Collider (RHIC) was that production of high transverse momentum (p_T) hadrons in $\text{Au}+\text{Au}$ collisions is strongly suppressed compared to that in $p+p$ collisions scaled by the number of binary collisions. This suppression indicates that partons experience substantial energy loss as they traverse the QGP, a phenomenon called jet-quenching [5]. A control experiment involving a deuteron projectile on a heavy-ion target, $d+\text{Au}$, was carried out to test whether the feature of strong energy loss is still present in a collision system of much smaller size. The results in $d+\text{Au}$ collisions at midrapidity presented in Ref. [6] showed no suppression at high p_T , initially leading to the conclusion that QGP itself—and associated jet quenching—were unique to collisions of larger heavy ions. In the ten years because these initial measurements, indications of QGP formation in smaller collision systems including $d+\text{Au}$ have been found, though without evidence of jet quenching phenomena [7].

Although there were no indications of strong suppression of high p_T particles in $d+\text{Au}$ collisions, detailed measurements do indicate other particle-production modifications relative to $p+p$ collisions [8–12]. At midrapidity, a centrality-dependent enhancement of charged hadron production was observed at intermediate p_T ($2 < p_T < 5 \text{ GeV}/c$) [11] in $d+\text{Au}$ collisions at $\sqrt{s_{NN}} = 200 \text{ GeV}$. These nuclear effects may be due to initial- and/or final-state multiple scatterings of incoming and outgoing partons [13, 14]. Processes such as radial flow [15] and recombination [16] developed for heavy-ion collisions were also investigated to explain a stronger enhancement of p and \bar{p} over π^\pm and K^\pm [11]. Recent results of collectivity amongst identified particles in small collision systems at RHIC and the Large Hadron Collider [7] have been also explained within the hydrodynamic evolution model [17, 18].

The study of particle production at forward and backward rapidity can provide additional information on nuclear effects such as initial-state energy loss [19] and modification of nuclear parton distribution functions (nPDF) [20–24]. Of particular interest are gluons at

small Bjorken x_{Bj} (fraction of the proton's longitudinal momentum carried by the parton), where the dramatic increase of gluon density leads to expectation of saturation. This is often described within the color glass condensate (CGC) framework [25]. A strong centrality dependent suppression of single and dihadron production has been observed at forward rapidity in $d+\text{Au}$ collisions at $\sqrt{s_{NN}} = 200 \text{ GeV}$ [8–10]. A CGC calculation provides a good description of the experimental data [26, 27]. Also, a perturbative quantum chromodynamics (pQCD) calculation considering coherent multiple scattering with small- x_{Bj} gluons reproduces the suppression of particle production at forward rapidity [19, 28]. Another very different explanation for the suppression at forward rapidity is that color fluctuation effects modify the size of the high- x_{Bj} partons in the proton [29, 30].

Accessible quark and gluon x_{Bj} ranges depend on the pseudorapidity (η) and transverse momentum of final state hadrons or jets. Therefore, measurements over a wide kinematic range are quite useful to further understand nuclear effects in small collision systems. PHENIX experiment has two muon spectrometers that provide wide coverage at forward ($x_{\text{Bj}} \approx 0.02$, shadowing region) and backward rapidity ($x_{\text{Bj}} \approx 0.1$, anti-shadowing region). In the previous study of nuclear effects on charged hadron production in $d+\text{Au}$ collisions at $\sqrt{s_{NN}} = 200 \text{ GeV}$ [31], a significant suppression was observed at forward rapidity in high multiplicity collisions compared to that in low multiplicity collisions, whereas a moderate enhancement is seen at backward rapidity. Although the direction of modification is consistent with the expectation from nPDF modification, no specific model comparison was presented.

High statistics data samples of $p+p$, $p+\text{Al}$, and $p+\text{Au}$ collisions at $\sqrt{s_{NN}} = 200 \text{ GeV}$ were collected in 2015 by PHENIX. These data samples combined with the availability of a new forward silicon vertex tracking detectors, which enable the selection of particle tracks coming from the collision point, significantly improved p_T and η resolutions. The charged hadron analysis with these data sets can extend the previous study in $d+\text{Au}$ collisions [31], and a comparison between $p+\text{Al}$ and $p+\text{Au}$ of very different size of nuclei can provide new information on nuclear effects on charged hadron production in $p+A$ collisions.

In this paper, we present nuclear modification factors of charged hadron production at forward and backward rapidity in $p+\text{Al}$ and $p+\text{Au}$ collisions at $\sqrt{s_{NN}} = 200 \text{ GeV}$ of various multiplicities. Section II describes the experimental setup and the data sets used in this analysis. Section III details the analysis methods.

* PHENIX Spokesperson: akiba@rcf.rhic.bnl.gov

† Deceased

Section IV discusses systematic uncertainties. Section V presents results and discussion. Section VI gives the summary and conclusions.

II. EXPERIMENTAL SETUP

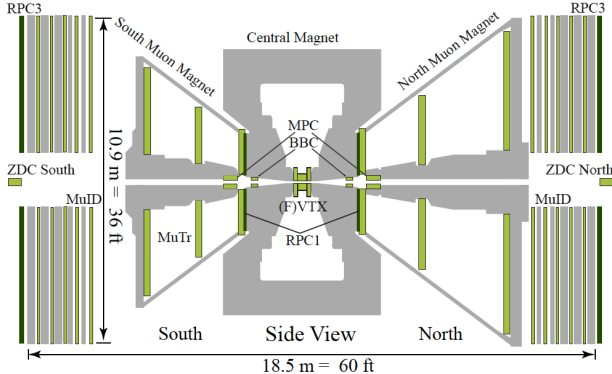


FIG. 1. Side view of the PHENIX detector in 2015.

The PHENIX detector [32] comprises two central arm spectrometers at midrapidity and two muon arm spectrometers at forward and backward rapidity. The detector configuration during the data taking in 2015 is shown in Fig. 1. The muon spectrometers have full-azimuthal acceptance, covering $-2.2 < \eta < -1.2$ (south arm) and $1.2 < \eta < 2.4$ (north arm). Each muon arm comprises a forward silicon vertex tracker (FVTX), followed by a hadron absorber and a muon spectrometer. The muon spectrometer is composed of a muon tracker (MuTr) embedded in a magnetic field followed by a muon identifier (MuID).

The FVTX is a silicon detector with four stations in each arm. Each station comprises 96 sensors along the ϕ direction. Each silicon sensor is finely segmented along the radial direction, with a strip pitch of $75 \mu\text{m}$. The primary purpose of the FVTX is to measure a precise collision vertex also constrained by the silicon vertex tracker (VTX) at midrapidity. The FVTX was also designed to measure precise momentum vector information of charged particles entering the muon spectrometer before suffering large multiple scattering in the hadron absorber. More technical details on the FVTX are available in Ref. [33]. Following the FVTX is the hadron absorber, composed of layers of copper, iron, and stainless steel, corresponding to 7.2 nuclear interaction lengths (λ_I). Hadrons entering the absorber are suppressed by a factor of approximately 1000, thus significantly reducing hadronic background for muon-based measurements.

The MuTr has two arms each consisting of three stations of cathode strip chambers, which are inside a magnet with a radial field integral of $\int B \cdot dl = 0.72 \text{ T}\cdot\text{m}$. The MuTr provides a momentum measurement for charged particles. The MuID is composed of five layers (referred

to as gap 0–4) of steel absorber (4.8 (5.4) λ_I for south (north) arm) and two planes of Iarocci tubes. This enables the separation of muons and hadrons based on their penetration depth at a given reconstructed momentum. The MuTr and MuID are also used to trigger events containing at least one muon or hadron candidate. The MuID trigger is designed to enrich events with muons by requiring at least one hit in either gap 3 or 4. Hadrons that stop only after partially penetrating the MuID can be enhanced by requiring no hit in gap 4. The MuTr trigger is used to sample high momentum tracks by requiring a track sagitta less than three MuTr cathode strips wide at the middle station of the MuTr. A more detailed discussion of the PHENIX muon arms can be found in Ref. [34, 35].

The beam-beam counters (BBC) [36] comprise two arrays of 64 quartz Čerenkov detectors located at $z = \pm 144 \text{ cm}$ from the nominal interaction point. Each BBC has an acceptance covering the full azimuth and $3.1 < |\eta| < 3.9$. The BBCs are used to determine the collision-vertex position along the beam axis (z_{BBC}) with a resolution of roughly 2 cm in $p+p$ collisions. They also provide a minimum bias (MB) trigger by requiring at least one hit in each BBC. The BBC trigger efficiency, determined from the Van der Meer scan technique [37], is 55% for inelastic $p+p$ events and 79% for events with midrapidity particle production [38]. In $p+\text{Al}$ and $p+\text{Au}$ collisions, charged particle multiplicity in BBC in the Al- and Au-going direction ($-4.9 < \eta < -3.1$) is used to categorize the event centrality. The BBC trigger is for 72% (84%) of inelastic $p+\text{Al}$ ($p+\text{Au}$) collisions. Centrality dependent bias factors to account for the efficiency for MB triggered events and hard scattering events have been obtained based on the method developed in Ref. [39].

III. DATA ANALYSIS

A. Data set

Data sets used in this analysis include $p+p$, $p+\text{Al}$, and $p+\text{Au}$ collisions at $\sqrt{s_{NN}} = 200 \text{ GeV}$ collected with the PHENIX detector in 2015. Events are required to have $|z_{\text{BBC}}| < 20 \text{ cm}$. The improved precision vertex from the silicon trackers (VTX and FVTX) is not used in this analysis due to the track multiplicity-dependent vertex reconstruction efficiency. The analyzed event samples are required to have at least one track candidate in the MuTr and MuID satisfying either single hadron or single muon trigger in coincidence with the MB trigger. The integrated luminosity of the data used in this analysis is 23 pb^{-1} in $p+p$, 260 nb^{-1} in $p+\text{Al}$, and 80 nb^{-1} in $p+\text{Au}$ collisions.

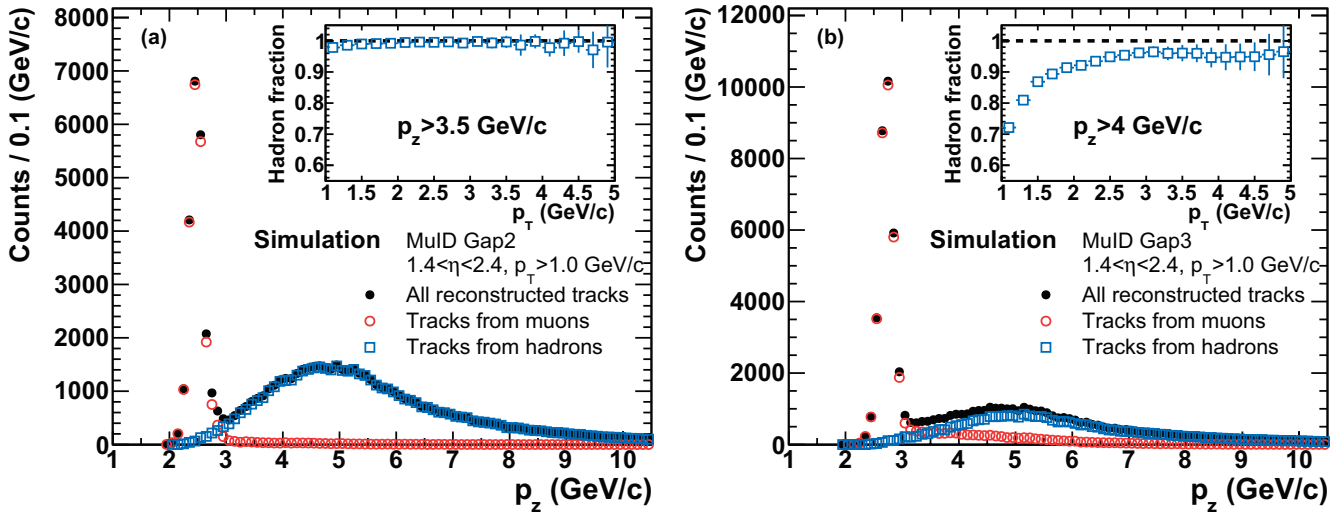


FIG. 2. GEANT4-detector-simulation results for the p_z distributions of reconstructed tracks at the MuID (a) gap 2 and (b) gap 3 in the north muon arm. The insets show the fraction of hadrons as a function of p_T with a p_z cut to help reject muon track candidates.

B. Hadron selection

The majority of hadrons emitted from the collision are stopped inside the hadron absorber. Hadrons which pass through the hadron absorber enter the MuTr and can still be stopped in the middle of the MuID by producing hadronic showers in the additional steel absorber planes. Low momentum muons can also be stopped due to ionization energy loss, but the momentum distribution measured in the MuTr is very different for these muons and hadrons which are stopped in the MuID. Figure 2 shows the longitudinal momentum (p_z) distributions of reconstructed tracks at the north arm MuID gaps 2 and 3 from a full GEANT4 detector simulation of charged hadrons (see Sec. III D). Muon tracks from light hadron decays show a narrow p_z distribution in $2.5 < p_z < 3.0$ GeV/c, whereas tracks from hadrons show a much broader distribution. Therefore, tracks from hadrons can be enriched with a proper p_z cut (3.5 GeV/c for gap 2 and 4 GeV/c for gap 3). The inset plots show the hadron fraction as a function of p_T with the p_z cuts. The hadron purity is $> 98\%$ ($> 90\%$) at MuID gap 2 (gap 3) for $p_T > 1.5$ GeV/c. The contamination of muons in the combined sample for both MuID gap 2 and gap 3 is less than 5% based on this simulation study.

One benefit from the FVTX is that the initial momentum vector of hadrons can be measured precisely before they undergo significant multiple scattering inside the absorber. In particular, the FVTX has very fine segmentation in the radial direction which can improve the p_T and η resolution of measured tracks, both of which are important for this analysis. Figure 3 shows the $\Delta\eta$ distribution between reconstructed tracks (η^{Reco}) and true tracks (η^{Gen}) as a function of p_T for hadron candidates from the GEANT4 simulation. In the case where momen-

tum information from only the MuTr is used, shown in Fig. 3 (a), the smearing in η is quite large. This is significantly improved by requiring association with FVTX tracks, shown in Fig. 3 (b).

C. Trigger efficiency

One consideration with the FVTX association requirement is the possibility of multiple FVTX tracks within the search window of a projected MuTr track, due to the higher FVTX track multiplicity and the smeared momentum information from the MuTr as shown in Fig. 3 (a). In this case, a MuTr track can be associated with a wrong FVTX track. This is referred to as a mis-association. Such mis-associations result in further smearing of the reconstructed p_T and η . The FVTX-MuTr association efficiency depends on the event multiplicity. The probability of mis-association can be evaluated with a data driven method developed in [40, 41] by associating a MuTr track with FVTX tracks from another event of similar FVTX track multiplicity. The same method has been used in this analysis, and the estimated fraction of mis-associations in the $p+p$ data is $\sim 1.5\%$ at $p_T \approx 1.5$ GeV/c and decreases down to $\sim 0.5\%$ at $p_T \approx 5$ GeV/c. In the 0%–5% highest multiplicity $p+Au$ collisions, the estimated fraction of mis-associations in the south arm (Au-going direction) is $\sim 3\%$ at $p_T \approx 1.5$ GeV/c and $\sim 1\%$ at $p_T \approx 5$ GeV/c, which is a factor of two higher than the estimate for $p+p$ collisions. The mis-association fraction is also checked with hadron simulation events embedded into real data events, and is consistent with the data driven values. The embedding simulation described in Sec. III D is used to take into account the multiplicity dependent FVTX-MuTr association efficiency.

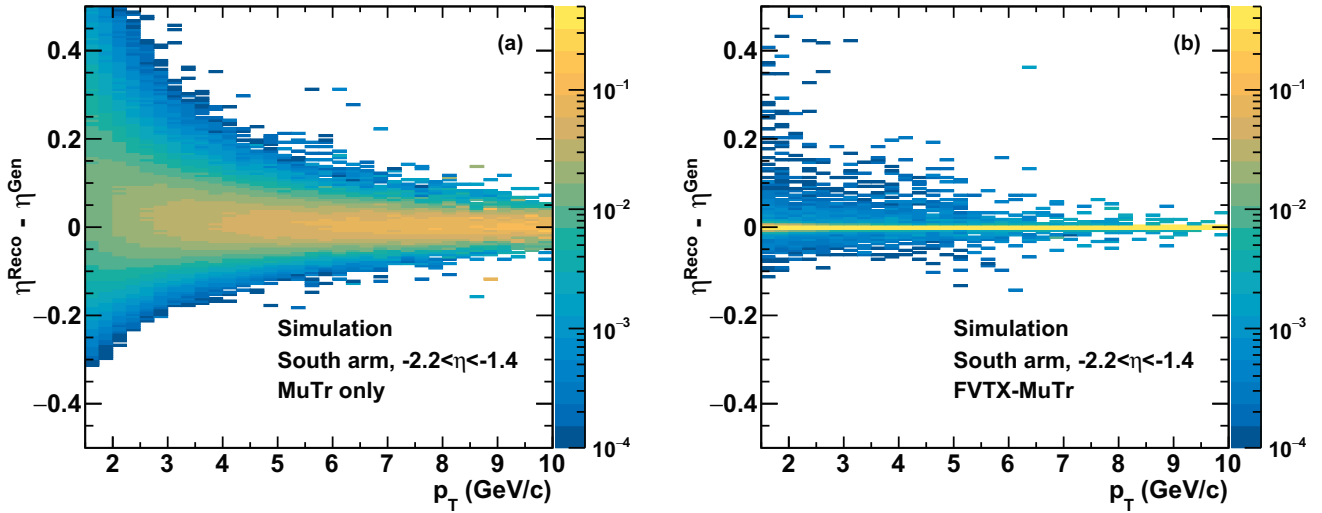


FIG. 3. Comparison of the p_T -dependent η resolution of tracks at MuID gap 2 and gap 3 in the south arm between tracks reconstructed with (a) MuTr only and (b) FVTX-MuTr association.

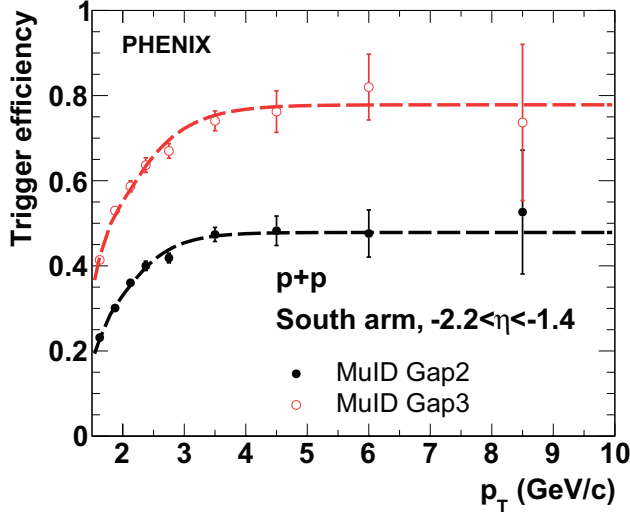


FIG. 4. Trigger efficiency of hadron candidates as a function of p_T in the south arm evaluated in $p+p$ collisions.

In addition to the requirements on p_z and FVTX-MuTr association, track quality cuts are applied. MuTr tracks are required to have at least 11 hits out of a maximum of 16 hits, and a 3σ MuTr track fit quality cut is applied. For association between MuTr and MuID tracks, three standard deviation cuts are applied to the angle and distance between MuTr and MuID tracks projected to the MuID gap 0. The associated FVTX track is required to have hits in at least three of the four stations, and an additional 3σ fit quality cut is applied. Momentum-dependent cuts are applied to the angle difference in the radial and azimuthal directions between FVTX and MuTr tracks projected to the middle of the absorber ($z = 70$ cm). These selections help reject tracks

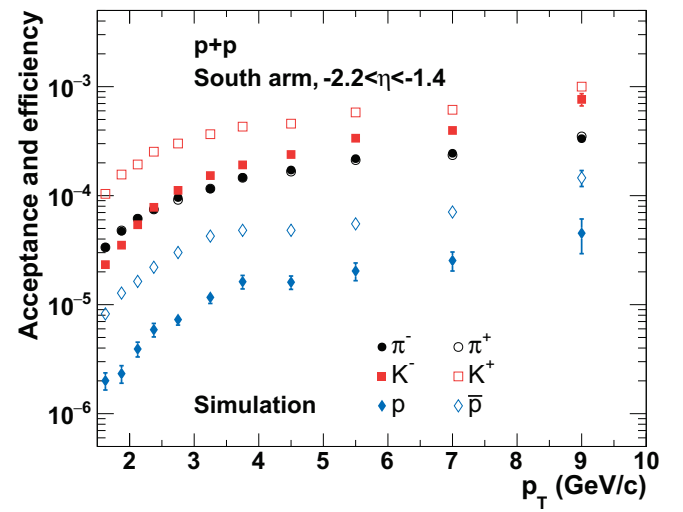


FIG. 5. Acceptance and reconstruction efficiency for different charged hadrons as a function of p_T in the south arm evaluated in $p+p$ collisions.

from decay muons, secondary hadrons, and FVTX-MuTr mis-associations.

The trigger efficiency is evaluated using hadron candidates from MB triggered events by measuring the fraction of hadron candidates satisfying the trigger requirements. Figure 4 shows the trigger efficiency for hadrons as a function of p_T at MuID gap 2 and gap 3 of the south arm in the $p+p$ data. The trigger efficiency for hadrons at MuID gap 3 is higher than that for hadrons at MuID gap 2. The efficiency at the north arm in the $p+p$ data is similar. Due to the larger statistical fluctuations at $p_T > 5$ GeV/c , a fit function is used to obtain the p_T -dependent trigger efficiency correction factors. The trig-

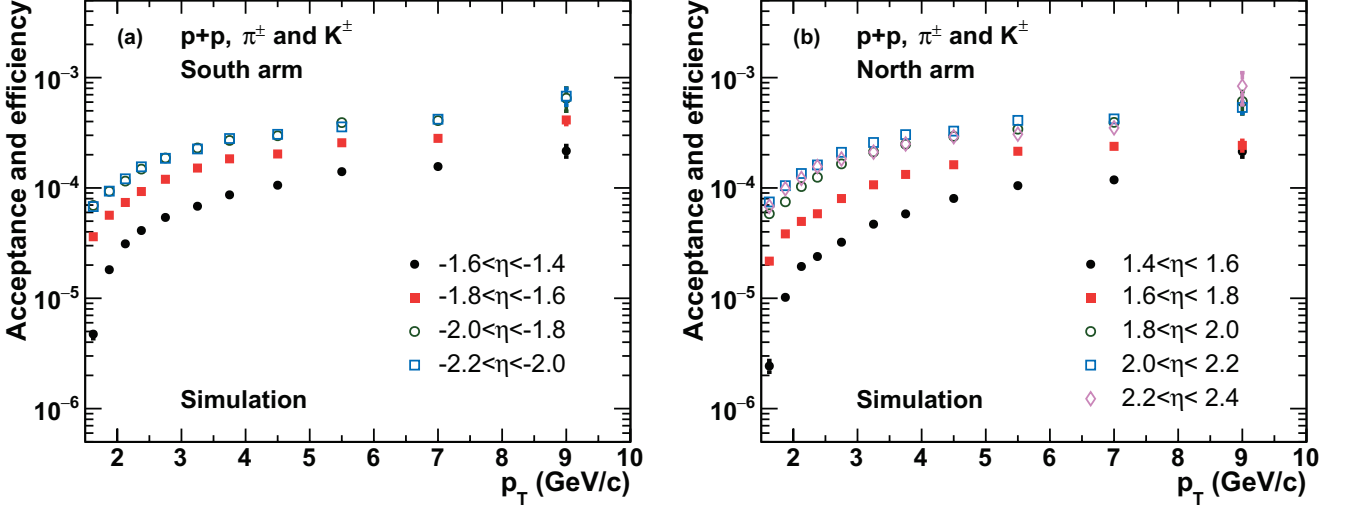


FIG. 6. Combined acceptance and reconstruction efficiency for π^\pm and K^\pm as a function of p_T in the (a) south and (b) north arms evaluated in $p+p$ collisions.

ger efficiency is separately evaluated for each muon arm as well as each centrality bin of $p+Al$ and $p+Au$ collisions to account for possible multiplicity effects and detector performance variation during the data taking period. The relative variation of the trigger efficiency over the data taking period is less than 10%. Because this variation of the trigger efficiency is accounted for by the detector performance variation described in Sec. III D, no additional systematic uncertainty is assigned.

D. Acceptance and reconstruction efficiency

Calculation of the absolute acceptance and efficiency for hadrons requires a detailed simulation of the hadronic interactions in the thick absorber material. There are significant uncertainties as observed from various GEANT4 implementations of such interactions. However, the response of hadrons inside the absorber is independent of collision systems, and hence this uncertainty will cancel out when comparing hadron yields between two collision systems. Therefore, nuclear effects on hadron production can be studied by taking into account only the additional multiplicity-dependent efficiency corrections. To obtain the multiplicity-dependent efficiency corrections, a full GEANT4 detector simulation was developed as follows:

1. Generate a mixture of hadrons (π^\pm , K^\pm , K_S^0 , K_L^0 , p , and \bar{p}) based on initial p_T and η distributions studied in [12, 42]. Based on measurements of identified charged hadrons at midrapidity [11, 43, 44], an extrapolation to forward and backward rapidity is done by multiplying the ratio of p_T spectra between mid and forward/backward rapidity from event generators [45, 46]. These simulated hadrons originate from a z distribution which matches the

measured z_{BBC} data.

2. Run a full GEANT4 simulation for the detector response of hadrons.
3. Reconstruct simulated detector hits embedded on top of background hits from real data for each centrality bin in each collision system. Apply the data-driven detector dead channel maps to account for variations in detector performance.

Figure 5 shows an example of acceptance and efficiency result as a function of p_T for different species of hadrons at MuID gaps 2 and 3 of the south arm in $p+p$ collisions. The acceptance and efficiency for π^\pm and K^- is comparable, and K^+ has the highest acceptance and efficiency due to its longer nuclear interaction length. The acceptance and efficiency for p and \bar{p} is much smaller than other charged hadrons.

Due to these species-dependent corrections, the overall acceptance and efficiency will depend on the relative production of these hadrons. In order to correctly account for the species dependence, an initial K^\pm/π^\pm ratio for each collision system is estimated separately. The contribution of p and \bar{p} to reconstructed tracks based on this hadron simulation is less than 5%, and thus we do not include them in the overall result. Figure 6 shows the combined acceptance and efficiency for π^\pm and K^\pm as a function of p_T in $p+p$ collisions for various η ranges. The acceptance and efficiency is higher at more forward rapidity where path length through the absorber is shorter, and the total momentum of tracks for a given p_T range is also larger. To have a more accurate correction, the full p_T and η dependent correction is applied.

E. Nuclear modification factor

Nuclear effects on charged hadron production in p +Al and p +Au collisions are quantified with the nuclear modification factor,

$$R_{pA} = \frac{dY^{pA}/dp_T d\eta}{dY^{pp}/dp_T d\eta} \cdot \frac{1}{\langle N_{\text{coll}} \rangle}, \quad (1)$$

where $dY^{pA}/dp_T d\eta$ is the charged hadron yield in a certain centrality bin of p +Al and p +Au collisions. These yields are corrected for the trigger efficiency, acceptance and reconstruction efficiency, and centrality bias factor introduced in Sec. II. $dY^{pp}/dp_T d\eta$ is the hadron yield in p + p collisions corrected for the trigger efficiency, acceptance and reconstruction efficiency, and BBC efficiency. Finally $\langle N_{\text{coll}} \rangle$ is the mean number of binary collisions for the corresponding centrality bin as calculated with the MC Glauber framework [47]. The $\langle N_{\text{coll}} \rangle$ values, bias correction factors, and related systematic uncertainties for each centrality bin of p +Al and p +Au collisions appear in Table I.

TABLE I. The $\langle N_{\text{coll}} \rangle$ and centrality bias correction factors are shown for different centrality selections of p +Al and p +Au collisions.

collision system	centrality	$\langle N_{\text{coll}} \rangle$	bias factor
p +Al	0%–5%	4.1 ± 0.4	0.75 ± 0.01
	5%–10%	3.5 ± 0.3	0.81 ± 0.01
	10%–20%	2.9 ± 0.3	0.84 ± 0.01
	20%–40%	2.4 ± 0.1	0.90 ± 0.02
	40%–72%	1.7 ± 0.1	1.04 ± 0.04
	0%–100%	2.1 ± 0.1	0.80 ± 0.02
p +Au	0%–5%	9.7 ± 0.6	0.86 ± 0.01
	5%–10%	8.4 ± 0.6	0.90 ± 0.01
	10%–20%	7.4 ± 0.5	0.94 ± 0.01
	20%–40%	6.1 ± 0.4	0.98 ± 0.01
	40%–60%	4.4 ± 0.3	1.03 ± 0.01
	60%–84%	2.6 ± 0.2	1.00 ± 0.06
	0%–100%	4.7 ± 0.3	0.86 ± 0.01

IV. SYSTEMATIC UNCERTAINTIES

In this section, sources of systematic uncertainty in the nuclear modification factor are described, and the procedure used to determine each systematic uncertainty is discussed.

A. Acceptance and efficiency

1. Initial hadron distribution

Because there are limited measurements of identified charged hadrons at forward and backward rapidity ($1.2 < |\eta| < 2.4$), some model assumptions are necessary. Such forward rapidity particle yields have previously been estimated for use in earlier PHENIX p + p and d +Au collisions studies—see Ref. [12] for details. Here we follow that previous work as input for our simulation studies. To account for uncertainties on the estimated p_T and η distributions, weight factors in p_T and η for each collision system are extracted by comparing reconstructed p_T and η distributions between data and simulation. The variation of acceptance and efficiency with modified initial p_T and η distributions based on the weighting factors is less than 3% for p + p data. For p +Al and p +Au data, the variation at forward (backward) rapidity is less than 3% (5%). The variation is included in the systematic uncertainty.

In addition, there is an uncertainty in the K^\pm/π^\pm ratio which influences the combined acceptance and efficiency due to the longer nuclear interaction length of K^+ . Based on the uncertainties of measurements at midrapidity [11, 43, 44] used as an input for extrapolation to forward and backward rapidity and a possible extrapolation uncertainty estimated by comparing with the data at more forward rapidity [48], an effect of a $\pm 30\%$ variation of K^\pm/π^\pm on the acceptance and efficiency has been evaluated.

The K^\pm/π^\pm at midrapidity in various centrality bins of d +Au collisions are compatible with each other [11], and the difference of K^\pm/π^\pm between d +Au and p +Al and p +Au collisions in HIJING [46] is less than 10%. These additional sources of uncertainty are covered by the 30% variation of K^\pm/π^\pm . The variation of acceptance and efficiency due to the 30% K^\pm/π^\pm change is less than 5% (7%) in p + p (p +Al and p +Au) collisions.

2. Proton contamination

As described in Sec. III D, the acceptance and efficiency is calculated for π^\pm and K^\pm . There is an $\sim 5\%$ proton contamination where the fraction may vary with the initial $p/(\pi + K)$ ratio. Based on the results in p + p and d +Au collisions at midrapidity [11, 43, 44], the p/π ratio at $p_T \approx 2 \text{ GeV}/c$ in 0%–20% central d +Au collisions is about 30% larger than in p + p collisions, which results in an increase of the contamination to 6.5% in 0%–20% central d +Au collisions as compared with 5% in p + p collisions. However, there is a lack of p/π measurements in a broader p_T range in various centrality ranges of p +Al and p +Au collisions. Therefore, a conservative uncertainty of 5% is assigned corresponding to a factor of two difference in $p/(\pi + K)$ ratios between p +Al, p +Au, and p + p collisions.

3. Hadron simulation

Although hadron response inside the absorber will not vary between different collision systems, the variation of acceptance and efficiency among three hadron interaction models (QGSP BERT, QGSP BIC, and FTFP BERT) in GEANT4 has been checked. A detailed description of the three models and a previous study for muons can be found in Refs. [49, 50]. The variation of the combined acceptance and efficiency for π^\pm and K^\pm between the three models is less than 2% in p_T and η .

4. Variation of detector efficiency

During the data taking period, the detector performance varied due to temporary dead channels, changes in the instantaneous beam luminosity, and other experimental factors. The average detector efficiency for each collision system is included in the hadron simulation. The raw yield variation in FVTX and muon tracks is considered as a source of systematic uncertainty. The level of variation appears in Table II. The FVTX performance is quite stable during the entire data taking period, and the variation of the muon arm is observed to be larger in the south arm in the p +Au data due to a larger sensitivity of the MuID efficiency to the instantaneous beam luminosity of Au ions. A 1σ variation of the raw yield is assigned as a systematic uncertainty for each detector, and two systematic uncertainties are added in quadrature.

TABLE II. Variation of detector performance for the south (S) and north (N) muon-arm spectrometers, as characterized by the number of FVTX and MuTr-MuID tracks per event.

Collision system	FVTX	MuTr-MuID
$p+p$	2.8%(S), 2.6%(N)	4.8%(S), 5.6%(N)
$p+Al$	2.4%(S), 2.1%(N)	3.0%(S), 2.8%(N)
$p+Au$	2.7%(S), 2.3%(N)	7.2%(S), 2.7%(N)

5. FVTX-MuTr mis-association

The probability of FVTX-MuTr mis-association depends on the FVTX track multiplicity, and the mis-association may artificially increase the acceptance and efficiency when requiring FVTX track association. The procedure for calculating the acceptance and efficiency using embedded simulations takes into account the multiplicity dependent FVTX-MuTr mis-association. The primary method to estimate the fraction of FVTX-MuTr is the data driven method described in Sec. III B, and the systematic uncertainty is evaluated by comparing with the estimated fraction from the embedded simulation. The difference is less than 1% of the maximum $\sim 3\%$

of FVTX-MuTr mis-association contamination in 0%–5% p +Au collisions. A 1% systematic uncertainty is assigned for the estimation of FVTX-MuTr mis-association.

6. Vertex resolution

Because the location of the FVTX is close to the interaction point, the η acceptance of the FVTX depends on the z position of collisions. In the hadron simulation for acceptance and efficiency calculation, the measured z_{BBC} distribution for each collision system is used, but there is uncertainty due to the resolution of z_{BBC} . When considering the 2 cm of z_{BBC} resolution, the variation of acceptance and efficiency is less than 0.5% in all three collision systems. A 0.5% systematic uncertainty is assigned due to the z_{BBC} resolution.

B. Contamination from secondary hadrons

Remaining secondary hadrons can introduce a smearing of kinematic variables (p_T and η) used in this analysis. The hadron simulation for calculating acceptance and efficiency already includes this component, however there can be a discrepancy in the relative contribution of secondary hadrons between the data and simulation. The systematic uncertainty on R_{pA} is estimated by varying the FVTX-MuTr matching quality cuts (projection angles between FVTX and MuTr tracks) which affect the remaining fraction of secondary hadrons. Based on the hadron simulation, a tighter or looser FVTX-MuTr matching quality cut changes the relative fraction of secondary hadrons by $\sim 25\%$; the variation on R_{pA} is less than 3%.

C. Multiple collisions

Due to the high instantaneous beam luminosity particularly in $p+p$ and $p+Al$ collisions, there is a chance of having multiple collisions in a single bunch crossing. This can introduce a bias in the yield calculation as well as centrality determination. The effect has been checked by analyzing two data groups with low and high instantaneous beam luminosity, and the difference in R_{pA} is less than 5%. The variation due to multiple collisions is already considered in the systematic uncertainty from the variations in detector efficiency with data-taking period. Therefore, no additional systematic uncertainty is assigned.

D. BBC efficiency and centrality selection

The BBC efficiency in $p+p$ collisions is $\sim 55\%$ for MB events and $\sim 79\%$ for hard scattering events, and

a 10% systematic uncertainty is assigned based on previous studies [38]. This uncertainty is a global scale uncertainty.

As described in Table I, there are systematic uncertainties on $\langle N_{\text{coll}} \rangle$ and bias correction factor calculations. The procedure to estimate these systematic uncertainties has been studied for $d+\text{Au}$ collisions [39], and the same procedure is used for $p+\text{Al}$ and $p+\text{Au}$ collisions.

E. Summary of systematic uncertainty

Table III shows the summary of systematic uncertainties. All systematic uncertainties are point-to-point correlated. Because most of sources on the acceptance and efficiency are independent in each collision system, there is no cancellation of systematic uncertainty for R_{pA} calculation.

TABLE III. Summary of systematic uncertainties.

Source	Relative uncertainty
Acceptance and efficiency	9.5–9.9% ($p+p$) 9.8–10.7% ($p+\text{Al}$) 9.8–12.6% ($p+\text{Au}$)
Secondary hadron	3%
BBC efficiency and centrality bias correction	10% ($p+p$) 1.3–4.2% ($p+\text{Al}$) 0.4–1.2% ($p+\text{Au}$)
$\langle N_{\text{coll}} \rangle$	4.7–8.5% ($p+\text{Al}$) 5.8–6.6% ($p+\text{Au}$)

V. RESULTS AND DISCUSSION

Figures 7 and 8 show R_{pA} of charged hadrons as a function of p_T at forward and backward rapidity in $p+\text{Al}$ and $p+\text{Au}$ collisions at $\sqrt{s_{\text{NN}}} = 200$ GeV. Both results in 0%–100% centrality are obtained by integrating over all centrality and applying the bias correction factors. Bars (boxes) around the data points represent statistical (systematic) uncertainties, and boxes around unity represent the global systematic uncertainty due to uncertainties in the BBC efficiency and the calculated $\langle N_{\text{coll}} \rangle$. The results for $p+\text{Al}$ indicate that there is little modification at forward rapidity (i.e. in the p -going direction), whereas a small enhancement is observed in $p_T < 2$ GeV/ c at backward rapidity (i.e. in the Al-going direction). In $p+\text{Au}$ results, a suppression is seen in $p_T < 3$ GeV/ c at forward rapidity unlike the $p+\text{Al}$ results. At backward rapidity, a similar trend of enhancement is observed in the $p+\text{Au}$ data, though with larger magnitude.

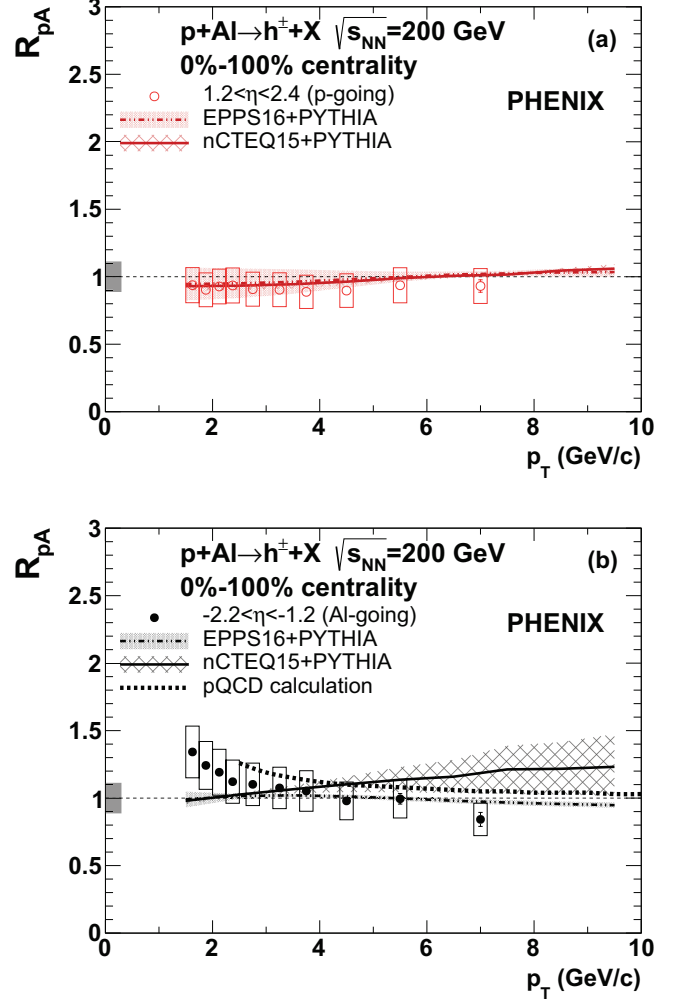


FIG. 7. R_{pA} of charged hadrons as a function of p_T at (a) forward and (b) backward rapidity in $p+\text{Al}$ 0%–100% centrality selected collisions at $\sqrt{s_{\text{NN}}} = 200$ GeV. Also shown are comparisons to a pQCD calculation [14] and calculations based on the nPDF sets [22, 23].

Comparisons with estimated R_{pA} based on nuclear modified PDFs are shown from the nCTEQ15 nPDF [22] and the EPPS16 nPDF [23] interfaced with PYTHIA v8.235 [51]; the parameters used in the event generation of PYTHIA are listed in Table IV. Note that the multiplication factor for multiparton interactions is determined by comparing the η -dependent multiplicity distribution in $p+p$ collisions at $\sqrt{s} = 200$ GeV [52]. The calculations indicate a modest expected suppression at forward rapidity from shadowing of low- x_{Bj} partons in the Au nucleus, and are in agreement with the data within uncertainties. However, at backward rapidity, sensitive to potential anti-shadowing of higher- x_{Bj} partons in the Au nucleus, the calculations result in no modification in contradistinction from the data. pQCD calculations considering incoherent multiple scatterings inside the nucleus

TABLE IV. Parameter used in PYTHIA8

parameter	value	description
SoftQCD:inelastic=on	on	QCD process for MB
PDF:pSet	7	CTEQ6L parton distribution function
MultipartonInteractions:Kfactor	0.5	Multiplication factor for multiparton interaction

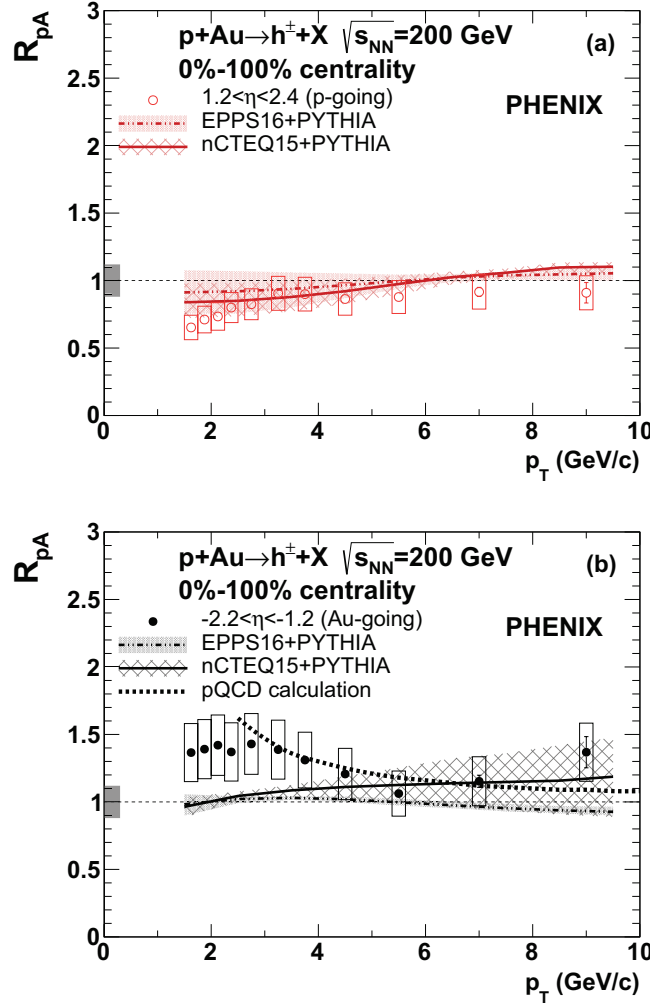


FIG. 8. R_{pA} of charged hadrons as a function of p_T at (a) forward and (b) backward rapidity in $p+Au$ 0%–100% centrality selected collisions at $\sqrt{s_{NN}} = 200$ GeV. Also shown are comparisons to a pQCD calculation [14] and calculations based on the nPDF sets [22, 23].

before and after hard scattering [14] at backward rapidity are also compared with the data, and it agrees with the both $p+Al$ and $p+Au$ data.

Figure 9 shows R_{pA} of charged hadrons integrated over the interval $2.5 < p_T < 5$ GeV/c as a function of η in the 0%–100% centrality selection of (a) $p+Al$ and (b) $p+Au$ collisions at $\sqrt{s_{NN}} = 200$ GeV. Again the data are compared with pQCD calculations at backward rapidity and

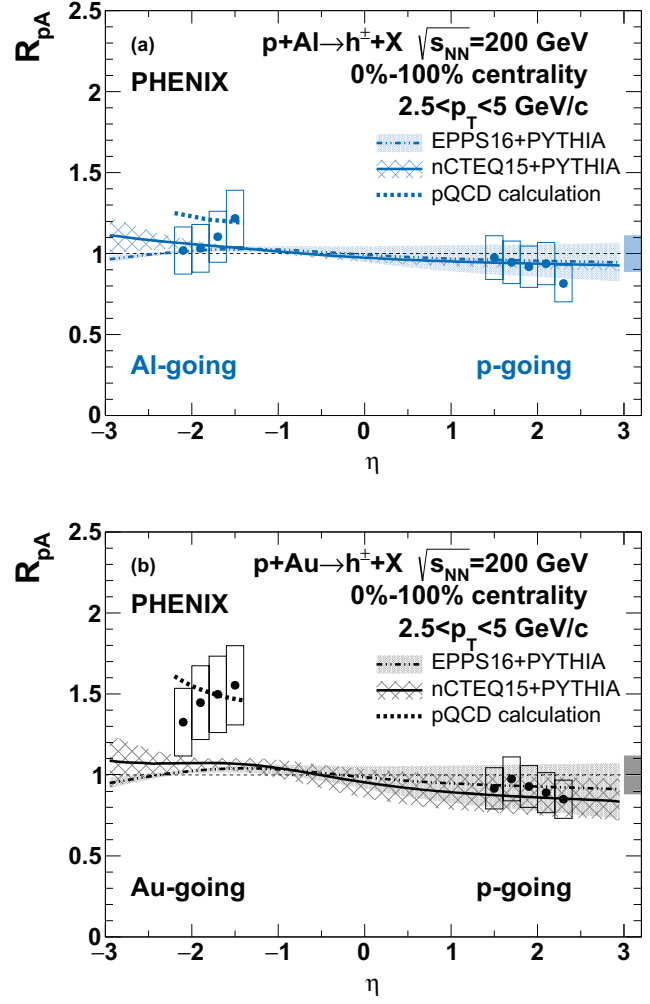


FIG. 9. R_{pA} of charged hadrons in $2.5 < p_T < 5$ GeV/c as a function of η in (a) $p+Al$ and (b) $p+Au$ 0%–100% centrality selected collisions at $\sqrt{s_{NN}} = 200$ GeV. Also shown are comparisons to a pQCD calculation [14] and calculations based on the nPDF sets [22, 23].

calculations based on two nPDF sets. In $p+Au$ collisions, there is a modest hint that enhancement at backward rapidity becomes larger as η approaches midrapidity, while the suppression at forward rapidity becomes stronger. In $p+Al$ collisions, R_{pA} at forward rapidity is quite similar to what is observed in $p+Au$ collisions, whereas it shows a smaller enhancement at backward rapidity than the results in $p+Au$ collisions. The comparison with

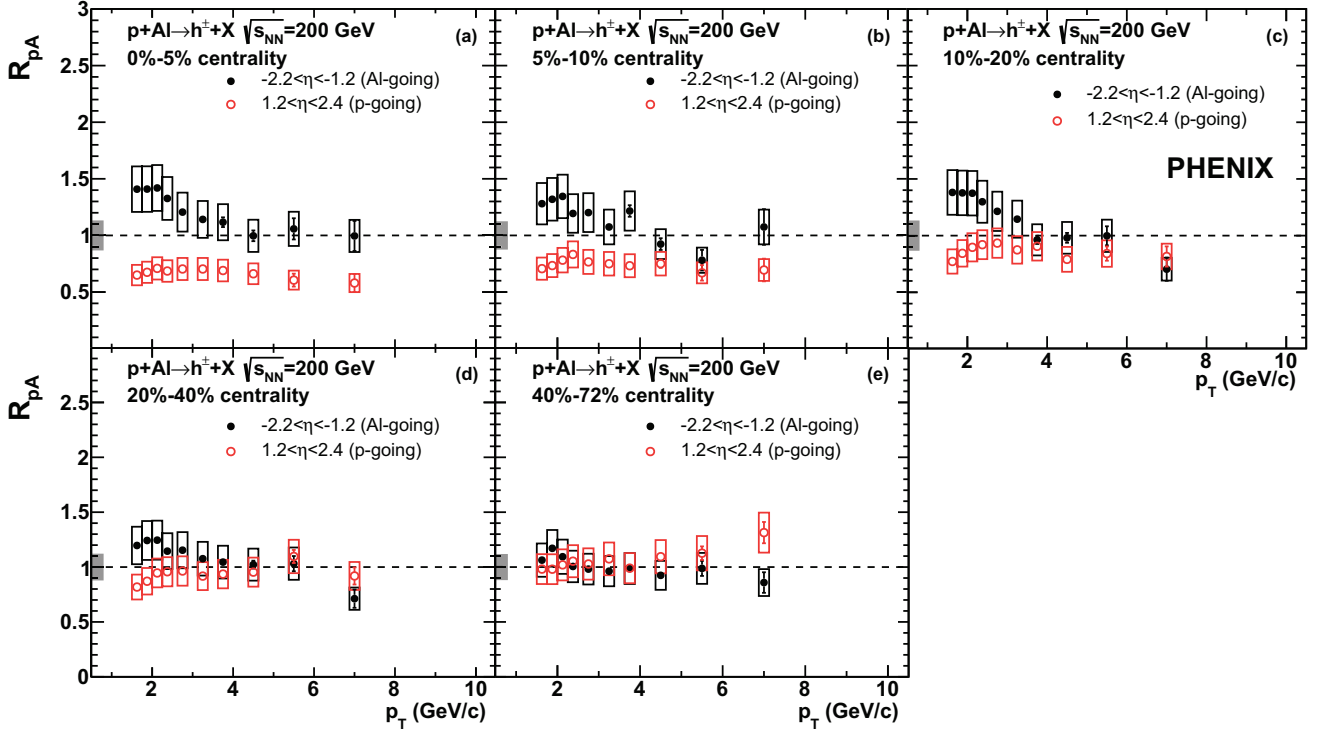


FIG. 10. R_{pA} of charged hadrons as a function of p_T at backward rapidity, $-2.2 < \eta < -1.2$, Al-going (filled [black] circles) and forward rapidity, $1.2 < \eta < 2.4$, p -going (open [red] circles) in various centrality classes of $p+Al$ collisions at $\sqrt{s_{NN}} = 200$ GeV.

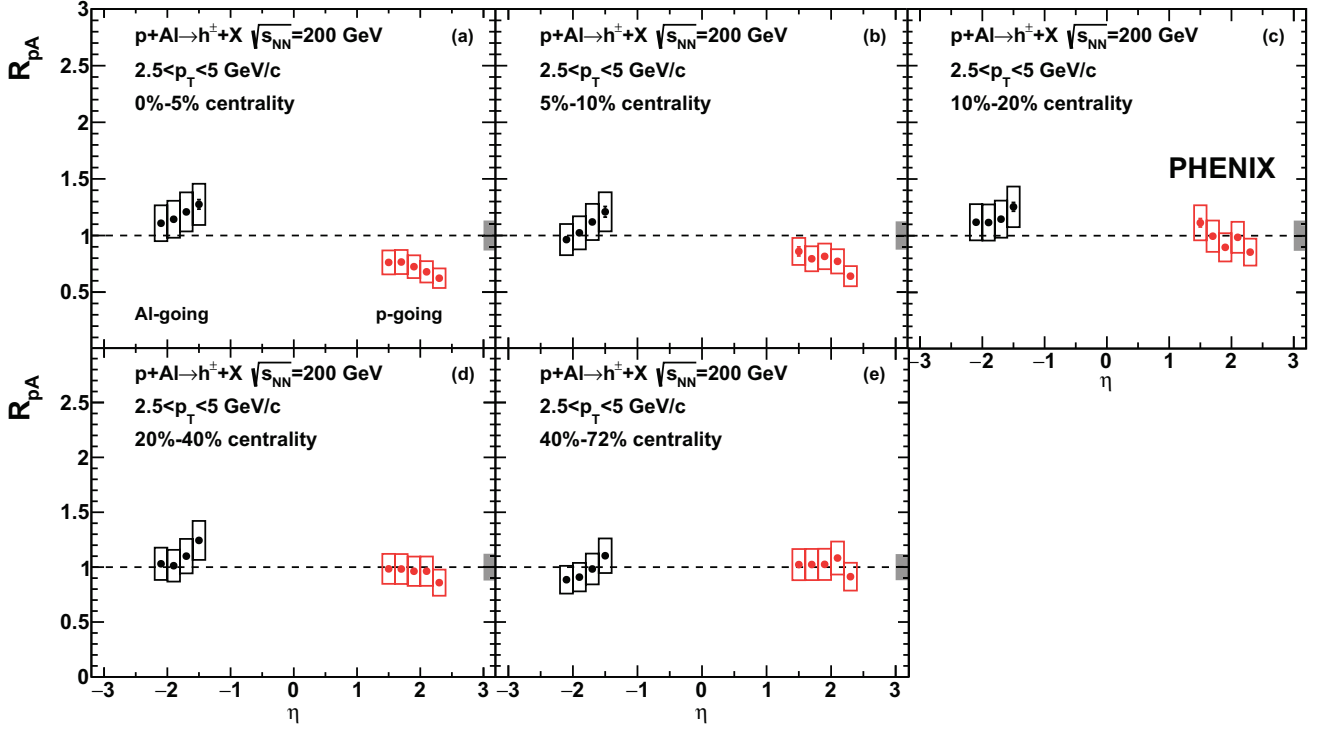


FIG. 11. R_{pA} of charged hadrons in $2.5 < p_T < 5$ GeV/c as a function of η in various centrality classes of $p+Al$ collisions at $\sqrt{s_{NN}} = 200$ GeV.

nCTEQ15 and EPPS16 nPDF calculations indicates that the R_{pA} at forward rapidity agrees in both $p+A$ and $p+A$ collisions, but the enhancement at backward rapidity in $p+A$ collisions is not reproduced by the both calculations. In case of the comparison with the pQCD calculations at backward rapidity, the magnitude of enhancement is similar. However, the pQCD calculations show a stronger enhancement at more backward rapidity which is different from the trend in the data.

Because initial and final-state nuclear effects on hadron production may depend on the density of initial partons in the nucleus and on the density of final-state produced particles, R_{pA} has been measured in various centrality bins of $p+A$ and $p+A$ collisions. Figures 10 and 11 show R_{pA} of charged hadrons as a function of p_T or η at forward and backward rapidity from the most central bin (0%–5%) to the most peripheral bin (40%–72%) for $p+A$ collisions at $\sqrt{s_{NN}} = 200$ GeV. The results at forward and backward rapidity are plotted together in each plot. First, there is a clear centrality dependence both at forward and backward rapidity. The magnitude of the modification, which shows enhancement at backward rapidity and suppression at forward rapidity, becomes stronger in more central $p+A$ collisions. The observed R_{pA} in the most peripheral (40%–72%) $p+A$ collisions is consistent with unity in both rapidity regions, indicating little modification of charged hadron production compared to the $p+p$ data. Both the magnitude of the modification and the p_T dependence are larger in central collisions. at forward and backward rapidity in central $p+A$ collisions. The centrality dependence of R_{pA} as a function of η shown in Fig. 11 is consistent with what is seen in R_{pA} as a function of p_T . The η dependence at backward rapidity is weakly centrality dependent, but there is a clear η dependence at forward rapidity in the most central collisions.

Figures 12 and 13 show R_{pA} of charged hadrons as a function of p_T and η in various centrality classes of $p+A$ collisions. Similar to the results in $p+A$ collisions, the magnitude of modification becomes larger in more central collisions both at forward and backward rapidity, and the R_{pA} values in the most peripheral $p+A$ collisions are consistent with unity. When comparing $p+A$ and $p+A$ results in the 0%–5% central collisions shown in the panel (a) of Figs. 10, 11, 12, and 13, R_{pA} at forward rapidity is comparable between the two collision systems. However, the enhancement at backward rapidity is much stronger in $p+A$ collisions. Figure 12 compares pQCD calculations with the $p+A$ data at backward rapidity. Similarly with the comparison in the integrated centrality, the calculation can reproduce the p_T and centrality dependent enhancement.

Figure 14 shows R_{pA} as a function of $\langle N_{\text{part}} \rangle$ for charged hadrons in the range $2.5 < p_T < 5$ GeV/c at (a) forward and (b) backward rapidity in $p+A$ and $p+A$ collisions at $\sqrt{s_{NN}} = 200$ GeV. Unlike the previous results, the systematic uncertainty on $\langle N_{\text{coll}} \rangle$ is included in boxes around data points. The data show that R_{pA}

at backward rapidity (filled [black] circles), i.e. in the A -going direction, increases monotonically with $\langle N_{\text{part}} \rangle$, and the trend is reproduced by the pQCD calculation. However, R_{pA} at forward rapidity (open [red] circles), i.e. in the p -going direction, reveal that each collision system has its own decreasing trend as $\langle N_{\text{part}} \rangle$ becomes larger. R_{pA} at forward rapidity in 0%–5% of $p+A$ and $p+A$ collisions are consistent ($R_{pA} \sim 0.7$), although $\langle N_{\text{part}} \rangle$ (9.7 in $p+A$ and 4.1 in $p+A$ collisions) are quite different. The trend of a larger enhancement (suppression) at backward (forward) rapidity in more central collisions is consistent with the previous results of charged hadrons and muons from heavy flavor decay in $d+A$ collisions [12, 31]. A closer look on η -dependent R_{pA} in 0%–5% $p+A$ and 40%–60% $p+A$ collisions of similar $\langle N_{\text{part}} \rangle$ is shown in Fig. 15. At backward rapidity, it shows not only a consistent magnitude of R_{pA} but also a quite similar trend of R_{pA} in η . In case of the comparison at forward rapidity, R_{pA} of the 40%–60% $p+A$ centrality bin is consistent with unity in all η bins, whereas a η -dependent suppression is seen in 0%–5% $p+A$ collisions.

The suppression of charged hadron production at forward rapidity in integrated centrality of $p+A$ and $p+A$ collisions can be explained by the nPDF modification based on the comparison with the nCTEQ15 and EPPS16 calculations shown in Figs 7, 8, and 9. It would be useful to extend another calculation within the CGC framework [27], which successfully describes the suppression of charged hadron production at forward rapidity in $d+A$ collisions [8, 9]. More differential calculations from these various frameworks are needed to compare to the systematic trends found in our new results. In addition to these models which consider modification of the parton distribution functions inside the nucleus, the pQCD calculation of dynamic shadowing considering coherent multiple scatterings inside the nucleus [19] also predicts a rapidity and impact parameter dependent suppression of hadron production at forward rapidity. The centrality dependent suppression at forward rapidity shown in both $p+A$ and $p+A$ collisions also can be described by the color fluctuation effects expecting a stronger centrality dependence in $p+A$ collisions than $d+A$ collisions [30]. It will be quite useful to have theoretical calculations for detailed comparison with the data in p_T , rapidity, and centrality.

For the enhancement of charged hadron production observed at backward rapidity, estimates from the nPDF sets clearly fail to describe the data. A pQCD calculation considering incoherent multiple scatterings both before and after hard scattering [14], which can describe the enhancement of heavy quark production at backward rapidity in $d+A$ collisions [12], successfully explains the centrality and A -dependent enhancement. In addition, there is also a possibility of hydrodynamic behavior showing a larger elliptic flow of charged particles at backward rapidity where the multiplicity is also larger than other rapidity ranges [53].

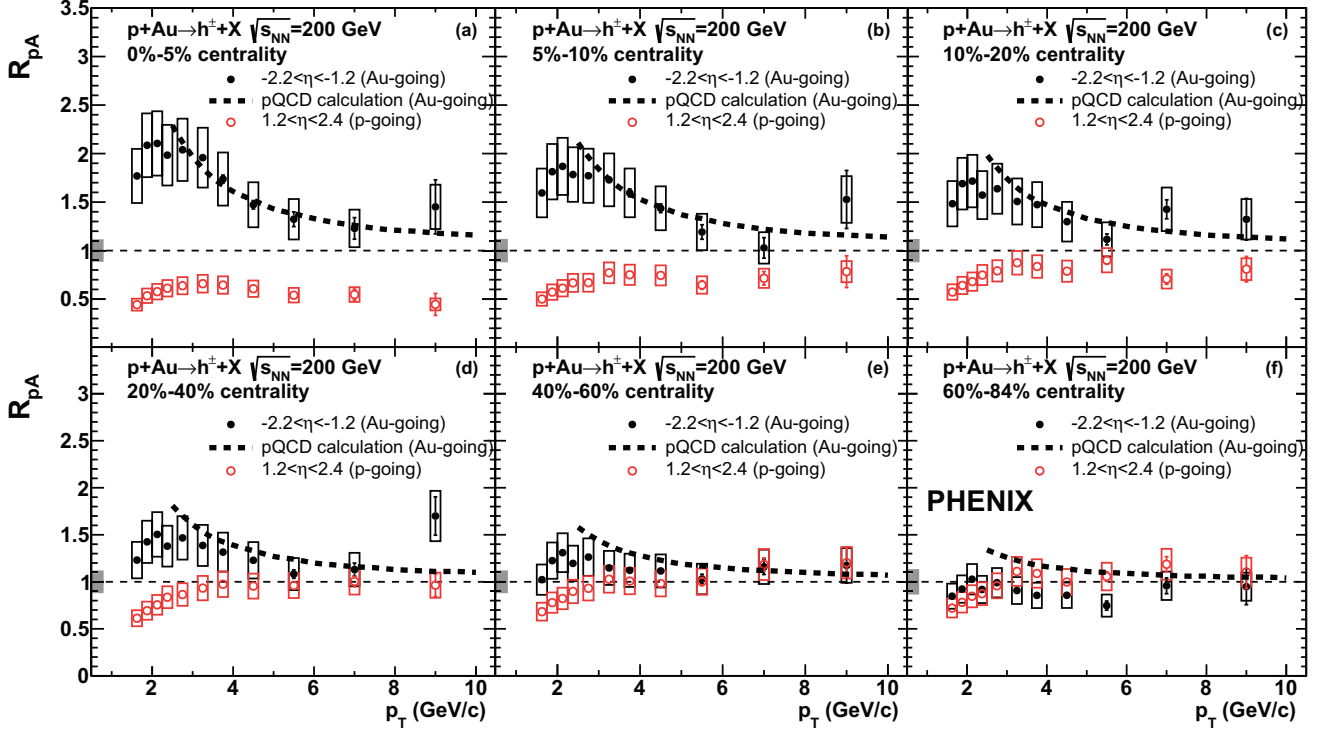


FIG. 12. R_{pA} of charged hadrons as a function of p_T at backward rapidity, $-2.2 < \eta < -1.2$, Au-going (filled [black] circles) and forward rapidity, $1.4 < \eta < 2.4$, p -going (open [red] circles) in various centrality classes of $p+Au$ collisions at $\sqrt{s_{NN}} = 200$ GeV.

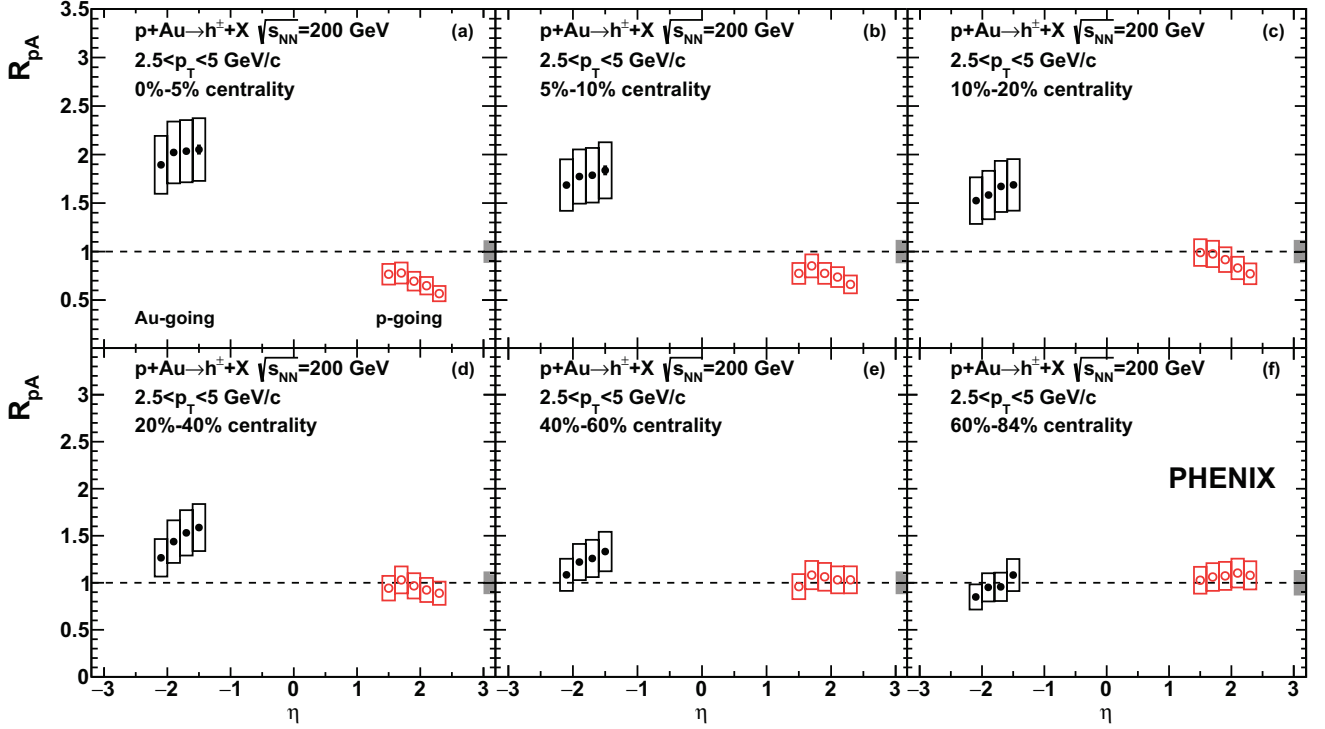


FIG. 13. R_{pA} of charged hadrons in $2.5 < p_T < 5$ GeV/c as a function of η in various centrality classes of $p+Au$ collisions at $\sqrt{s_{NN}} = 200$ GeV. Also shown are comparisons to a pQCD calculation [14].

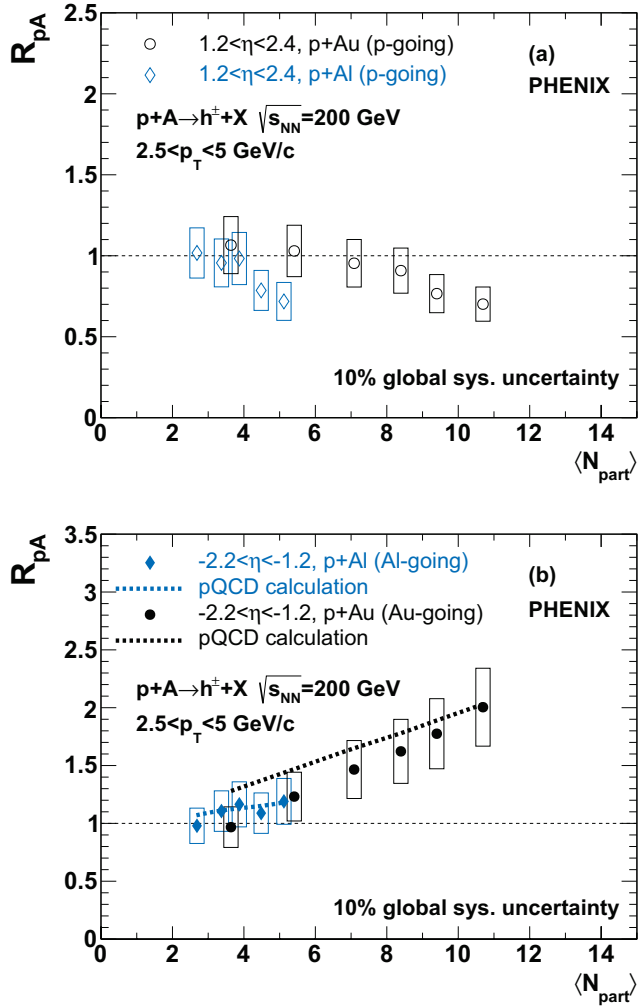


FIG. 14. R_{pA} of charged hadrons in $2.5 < p_T < 5$ GeV/c as a function of $\langle N_{\text{part}} \rangle$ at forward and backward rapidity in $p+\text{Al}$ and $p+\text{Au}$ collisions at $\sqrt{s_{\text{NN}}} = 200$ GeV. Also shown are comparisons to a pQCD calculation [14].

VI. SUMMARY

PHENIX has measured the nuclear modification factor R_{pA} of charged hadrons as a function of p_T and η at forward and backward rapidity in various centrality ranges of $p+\text{Al}$ and $p+\text{Au}$ collisions at $\sqrt{s_{\text{NN}}} = 200$ GeV. The results in central $p+\text{Al}$ and $p+\text{Au}$ collisions show a suppression (enhancement) in the forward p -going (backward, A -going) rapidity region compared to the binary scaled $p+p$ results of 0.7 (2.0) for $p+\text{Au}$ and 0.9 (1.2) for $p+\text{Al}$ in $2.5 < p_T < 5$ GeV/c at a level of significance 3.3σ (3.2σ) for $p+\text{Au}$ and 2.7σ (1.1σ) for $p+\text{Al}$. In contrast, there is no significant modification of charged hadron production observed in peripheral $p+\text{Al}$ and $p+\text{Au}$ collisions in either rapidity region. The enhancement at backward rapidity shows a clear A -dependence, but the suppression at forward rapidity is comparable

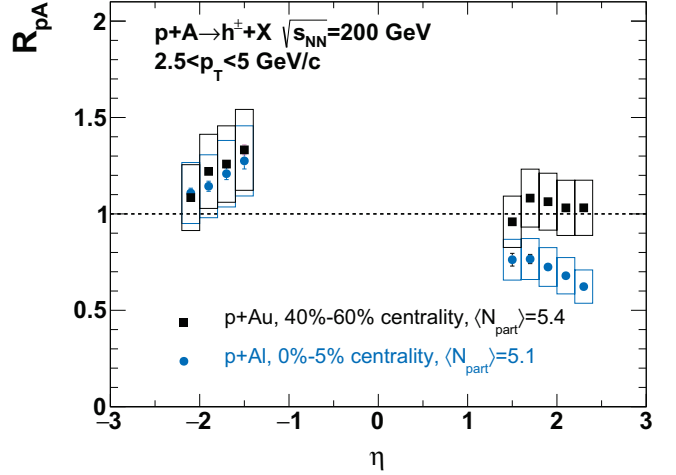


FIG. 15. R_{pA} of charged hadrons in $2.5 < p_T < 5$ GeV/c as a function of η in 0%–5% $p+\text{Al}$ and 40%–60% $p+\text{Au}$ collisions at $\sqrt{s_{\text{NN}}} = 200$ GeV of similar $\langle N_{\text{part}} \rangle$.

between the two collision systems despite more than a factor two larger $\langle N_{\text{part}} \rangle$ in $p+\text{Au}$ collisions. The results integrated over centrality are compared to a calculation with the nCTEQ15 and EPPS16 nPDF sets. The calculation agrees with the data at forward rapidity both in the integrated centrality of $p+\text{Al}$ and $p+\text{Au}$ collisions, but it fails to describe the enhancement observed at backward rapidity in $p+\text{Au}$ collisions. Because the nPDF sets does not yet provide an impact parameter dependent nPDF, the comparison is limited to the case of integrated centrality. These data measured in various centrality ranges can be useful to test impact parameter dependent nPDFs in different nuclei in the future. The pQCD calculation considering incoherent multiple scatterings inside the nucleus can describe the data at backward rapidity. In addition, a comparison with different models can help to improve the understanding of nuclear effects in small collision systems.

ACKNOWLEDGMENTS

We thank the staff of the Collider-Accelerator and Physics Departments at Brookhaven National Laboratory and the staff of the other PHENIX participating institutions for their vital contributions. We thank Z.-B. Kang and H. Xing for useful discussions and for providing theoretical calculations. We acknowledge support from the Office of Nuclear Physics in the Office of Science of the Department of Energy, the National Science Foundation, Abilene Christian University Research Council, Research Foundation of SUNY, and Dean of the College of Arts and Sciences, Vanderbilt University (U.S.A), Ministry of Education, Culture, Sports, Science, and Technology and the Japan Society for the Promotion

of Science (Japan), Conselho Nacional de Desenvolvimento Científico e Tecnológico and Fundação de Amparo à Pesquisa do Estado de São Paulo (Brazil), Natural Science Foundation of China (People's Republic of China), Croatian Science Foundation and Ministry of Science and Education (Croatia), Ministry of Education, Youth and Sports (Czech Republic), Centre National de la Recherche Scientifique, Commissariat à l'Énergie Atomique, and Institut National de Physique Nucléaire et de Physique des Particules (France), Bundesministerium für Bildung und Forschung, Deutscher Akademischer Austausch Dienst, and Alexander von Humboldt Stiftung (Germany), J. Bolyai Research Scholarship, EFOP, the New National Excellence Program (ÚNKP), NKFIH, and

OTKA (Hungary), Department of Atomic Energy and Department of Science and Technology (India), Israel Science Foundation (Israel), Basic Science Research and SRC(CENuM) Programs through NRF funded by the Ministry of Education and the Ministry of Science and ICT (Korea). Physics Department, Lahore University of Management Sciences (Pakistan), Ministry of Education and Science, Russian Academy of Sciences, Federal Agency of Atomic Energy (Russia), VR and Wallenberg Foundation (Sweden), the U.S. Civilian Research and Development Foundation for the Independent States of the Former Soviet Union, the Hungarian American Enterprise Scholarship Fund, the US-Hungarian Fulbright Foundation, and the US-Israel Binational Science Foundation.

[1] K. Adcox *et al.* (PHENIX Collaboration), Formation of dense partonic matter in relativistic nucleus-nucleus collisions at RHIC: Experimental evaluation by the PHENIX collaboration, *Nucl. Phys. A* **757**, 184 (2005).

[2] J. Adams *et al.* (STAR Collaboration), Experimental and theoretical challenges in the search for the quark gluon plasma: The STAR Collaboration's critical assessment of the evidence from RHIC collisions, *Nucl. Phys. A* **757**, 102 (2005).

[3] B. B. Back *et al.* (PHOBOS Collaboration), The PHOBOS perspective on discoveries at RHIC, *Nucl. Phys. A* **757**, 28 (2005).

[4] I. Arsene *et al.* (BRAHMS Collaboration), Quark gluon plasma and color glass condensate at RHIC? The Perspective from the BRAHMS experiment, *Nucl. Phys. A* **757**, 1 (2005).

[5] M. Gyulassy, I. Vitev, X.-N. Wang, and B.-W. Zhang, *Jet quenching and radiative energy loss in dense nuclear matter*, Quark Gluon Plasma, Vol. 3 (World Scientific, Singapore, 2003) pp. 123–191.

[6] S. S. Adler *et al.* (PHENIX Collaboration), Absence of suppression in particle production at large transverse momentum in $\sqrt{s_{NN}} = 200$ GeV d +Au collisions, *Phys. Rev. Lett.* **91**, 072303 (2003).

[7] J. L. Nagle and W. A. Zajc, Small System Collectivity in Relativistic Hadronic and Nuclear Collisions, *Ann. Rev. Nucl. Part. Sci.* **68**, 211 (2018).

[8] I. Arsene *et al.* (BRAHMS Collaboration), On the evolution of the nuclear modification factors with rapidity and centrality in d +Au collisions at $\sqrt{s_{NN}}=200$ GeV, *Phys. Rev. Lett.* **93**, 242303 (2004).

[9] J. Adams *et al.* (STAR Collaboration), Forward neutral pion production in p + p and d +Au collisions at $\sqrt{s_{NN}} = 200$ GeV, *Phys. Rev. Lett.* **97**, 152302 (2006).

[10] A. Adare *et al.* (PHENIX Collaboration), Suppression of back-to-back hadron pairs at forward rapidity in d +Au Collisions at $\sqrt{s_{NN}} = 200$ GeV, *Phys. Rev. Lett.* **107**, 172301 (2011).

[11] A. Adare *et al.* (PHENIX Collaboration), Spectra and ratios of identified particles in Au+Au and d +Au collisions at $\sqrt{s_{NN}} = 200$ GeV, *Phys. Rev. C* **88**, 024906 (2013).

[12] A. Adare *et al.* (PHENIX Collaboration), Cold-Nuclear-Matter Effects on Heavy-Quark Production at Forward and Backward Rapidity in d +Au Collisions at $\sqrt{s_{NN}} = 200$ GeV, *Phys. Rev. Lett.* **112**, 252301 (2014).

[13] A. Accardi, Cronin effect in proton-nucleus collisions: A Survey of theoretical models (2002), arXiv:hep-ph/0212148.

[14] Z.-B. Kang, I. Vitev, E. Wang, H. Xing, and C. Zhang, Multiple scattering effects on heavy meson production in p + A collisions at backward rapidity, *Phys. Lett. B* **740**, 23 (2015).

[15] T. Hirano and Y. Nara, Interplay between soft and hard hadronic components for identified hadrons in relativistic heavy ion collisions at RHIC, *Phys. Rev. C* **69**, 034908 (2004).

[16] R. C. Hwa and C. B. Yang, Scaling behavior at high p_T and the p/π ratio, *Phys. Rev. C* **67**, 034902 (2003).

[17] M. Habich, J. L. Nagle, and P. Romatschke, Particle spectra and HBT radii for simulated central nuclear collisions of C+C, Al+Al, Cu+Cu, Au+Au, and Pb+Pb from $\sqrt{s} = 62.4$ –2760 GeV, *Eur. Phys. J. C* **75**, 15 (2015).

[18] C. Shen, J.-F. Paquet, G. S. Denicol, S. Jeon, and C. Gale, Collectivity and electromagnetic radiation in small systems, *Phys. Rev. C* **95**, 014906 (2017).

[19] J. Qiu and I. Vitev, Coherent QCD multiple scattering in proton-nucleus collisions, *Phys. Lett. B* **632**, 507 (2006).

[20] D. F. Geesaman, K. Saito, and A. W. Thomas, The nuclear EMC effect, *Ann. Rev. Nucl. Part. Sci.* **45**, 337 (1995).

[21] D. de Florian, R. Sassot, P. Zurita, and M. Stratmann, Global Analysis of Nuclear Parton Distributions, *Phys. Rev. D* **85**, 074028 (2012).

[22] K. Kovarik *et al.*, nCTEQ15- Global analysis of nuclear parton distributions with uncertainties in the CTEQ framework, *Phys. Rev. D* **93**, 085037 (2016).

[23] K. J. Eskola, P. Paaikkinen, H. Paukkunen, and C. A. Salgado, EPPS16: Nuclear parton distributions with LHC data, *Eur. Phys. J. C* **77**, 163 (2017).

[24] R. Abdul Khalek, J. J. Ethier, and J. Rojo, Nuclear Parton Distributions from Lepton-Nucleus Scattering and the Impact of an Electron-Ion Collider, *Eur. Phys. J. C* **79**, 471 (2019).

[25] L. D. McLerran and R. Venugopalan, Gluon distribution functions for very large nuclei at small transverse momentum, *Phys. Rev. D* **49**, 3352 (1994).

[26] C. Marquet, Forward inclusive dijet production and azimuthal correlations in pA collisions, *Nucl. Phys. A* **796**, 41 (2007).

[27] J. L. Albacete and C. Marquet, Single Inclusive Hadron Production at RHIC and the LHC from the Color Glass Condensate, *Phys. Lett. B* **687**, 174 (2010).

[28] Z.-B. Kang, I. Vitev, and H. Xing, Dihadron momentum imbalance and correlations in $d+A$ collisions, *Phys. Rev. D* **85**, 054024 (2012).

[29] M. Alvioli, B. A. Cole, L. Frankfurt, D. V. Perepelitsa, and M. Strikman, Evidence for x -dependent proton color fluctuations in pA collisions at the CERN Large Hadron Collider, *Phys. Rev. C* **93**, 011902(R) (2016).

[30] M. Alvioli, L. Frankfurt, D. V. Perepelitsa, and M. Strikman, Global analysis of color fluctuation effects in proton- and deuteron-nucleus collisions at RHIC and the LHC, *Phys. Rev. D* **98**, 071502(R) (2018).

[31] S. S. Adler *et al.* (PHENIX Collaboration), Nuclear modification factors for hadrons at forward and backward rapidities in deuteron-gold collisions at $\sqrt{s_{NN}}=200$ GeV, *Phys. Rev. Lett.* **94**, 082302 (2005).

[32] K. Adcox *et al.* (PHENIX Collaboration), PHENIX detector overview, *Nucl. Instrum. Methods Phys. Res., Sec. A* **499**, 469 (2003).

[33] C. Aidala *et al.* (PHENIX Collaboration), The PHENIX Forward Silicon Vertex Detector, *Nucl. Instrum. Methods Phys. Res., Sec. A* **755**, 44 (2014).

[34] H. Akikawa *et al.* (PHENIX Collaboration), PHENIX muon arms, *Nucl. Instrum. Methods Phys. Res., Sec. A* **499**, 537 (2003).

[35] S. Adachi *et al.* (PHENIX Collaboration), Trigger electronics upgrade of PHENIX muon tracker, *Nucl. Instrum. Methods Phys. Res., Sec. A* **703**, 114 (2013).

[36] M. Allen *et al.* (PHENIX Collaboration), PHENIX inner detectors, *Nucl. Instrum. Methods Phys. Res., Sec. A* **499**, 549 (2003).

[37] A. Drees, B. Fox, Z. Xu, and H. Huang, Results from Vernier Scans at RHIC during the pp Run 2001-2002, *Conf. Proc. C* **030512**, 1688 (2003), Particle Accelerator Conference, PAC 2003, Portland, USA, May 12-16, 2003.

[38] S. S. Adler *et al.* (PHENIX Collaboration), Mid-rapidity neutral pion production in proton-proton collisions at $\sqrt{s}=200$ GeV, *Phys. Rev. Lett.* **91**, 241803 (2003).

[39] A. Adare *et al.* (PHENIX Collaboration), Centrality categorization for $R_{p(d)+A}$ in high-energy collisions, *Phys. Rev. C* **90**, 034902 (2014).

[40] C. Aidala *et al.* (PHENIX Collaboration), B -meson production at forward and backward rapidity in $p+p$ and Cu+Au collisions at $\sqrt{s_{NN}} = 200$ GeV, *Phys. Rev. C* **96**, 064901 (2017).

[41] C. Aidala *et al.* (PHENIX Collaboration), Measurements of $B \rightarrow J/\psi$ at forward rapidity in $p+p$ collisions at $\sqrt{s} = 510$ GeV, *Phys. Rev. D* **95**, 092002 (2017).

[42] A. Adare *et al.* (PHENIX Collaboration), Nuclear-Modification Factor for Open-Heavy-Flavor Production at Forward Rapidity in Cu+Cu Collisions at $\sqrt{s_{NN}} = 200$ GeV, *Phys. Rev. C* **86**, 024909 (2012).

[43] A. Adare *et al.* (PHENIX Collaboration), Identified charged hadron production in $p+p$ collisions at $\sqrt{s} = 200$ and 62.4 GeV, *Phys. Rev. C* **83**, 064903 (2011).

[44] G. Agakishiev *et al.* (STAR Collaboration), Identified hadron compositions in $p+p$ and Au+Au collisions at high transverse momenta at $\sqrt{s_{NN}} = 200$ GeV, *Phys. Rev. Lett.* **108**, 072302 (2012).

[45] T. Sjöstrand, S. Mrenna, and P. Z. Skands, PYTHIA 6.4 Physics and Manual (2006), *J. High Energy Phys.* **05** (2006) 026.

[46] M. Gyulassy and X.-N. Wang, HIJING 1.0: A Monte Carlo program for parton and particle production in high-energy hadronic and nuclear collisions, *Comput. Phys. Commun.* **83**, 307 (1994).

[47] C. Loizides, J. Nagle, and P. Steinberg, Improved version of the PHOBOS Glauber Monte Carlo, *SoftwareX* **1-2**, 13 (2015).

[48] I. Arsene *et al.* (BRAHMS Collaboration), Production of mesons and baryons at high rapidity and high p_T in proton-proton collisions at $\sqrt{s} = 200$ GeV, *Phys. Rev. Lett.* **98**, 252001 (2007).

[49] S. Agostinelli *et al.* (GEANT4 Collaboration), GEANT4: A Simulation toolkit, *Nucl. Instrum. Methods Phys. Res., Sec. A* **506**, 250 (2003).

[50] C. Aidala *et al.* (PHENIX Collaboration), Measurements of $\mu\mu$ pairs from open heavy flavor and Drell-Yan in $p+p$ collisions at $\sqrt{s} = 200$ GeV, *Phys. Rev. D* **99**, 072003 (2019).

[51] T. Sjöstrand, S. Ask, J. R. Christiansen, R. Corke, N. De-sai, P. Ilten, S. Mrenna, S. Prestel, C. O. Rasmussen, and P. Z. Skands, An Introduction to PYTHIA 8.2, *Comput. Phys. Commun.* **191**, 159 (2015).

[52] B. Alver *et al.* (PHOBOS Collaboration), Phobos results on charged particle multiplicity and pseudorapidity distributions in Au+Au, Cu+Cu, $d+A$, and $p+p$ collisions at ultra-relativistic energies, *Phys. Rev. C* **83**, 024913 (2011).

[53] A. Adare *et al.* (PHENIX Collaboration), Pseudorapidity dependence of particle production and elliptic flow in asymmetric nuclear collisions of $p+Al$, $p+Au$, $d+Au$, and ^3He+Au at $\sqrt{s_{NN}} = 200$ GeV, *Phys. Rev. Lett.* **121**, 222301 (2018).